Global
Biogeochemical Cycles

RESEARCH ARTICLE
10.1029/2019GB006380

This article is a companion to Rohr et al. (2020), https://doi.org/10.1029/2019GB006385

Eddy-Modified Iron, Light, and Phytoplankton Cell Division Rates in the Simulated Southern Ocean

Tyler Rohr[1,2], **Cheryl Harrison**[3,4,5], **Matthew C. Long**[5], **Peter Gaube**[6], **and Scott C. Doney**[1,7]

[1]Department of Marine Chemistry and Geochemistry, Woods Hole Oceanographic Institution, Woods Hole, MA, USA, [2]Department of Earth and Planetary Sciences, Massachusetts Institute of Technology, Cambridge, MA, USA, [3]School of Earth, Environmental and Marine Science, University of Texas Rio Grande Valley, Port Isabel Campus, Port Isabel, TX, USA, [4]Institute for Arctic and Alpine Research, University of Colorado, Boulder, CO, USA, [5]National Center for Atmospheric Research, Boulder, CO, USA, [6]Applied Physics Laboratory, University of Washington, Seattle, WA, USA, [7]Department of Environmental Sciences, University of Virginia, Charlottesville, VA, USA

Key Points:
- In the Southern Ocean, cyclonic and anticyclonic eddies preferentially exhibit depressed and enhanced iron concentrations, respectively
- Eddy-induced Ekman pumping is the dominant vertical transport mechanism for anomalous iron in these eddies
- Cyclones and anticyclones exhibit depressed and enhanced phytoplankton cell division rates, respectively, except in deep mixing waters

Supporting Information:
- Supporting Information S1

Correspondence to:
T. Rohr,
trohr@mit.edu

Citation:
Rohr, T., Harrison, C., Long, M. C., Gaube, P., & Doney, S. C. (2020). Eddy-modified iron, light, and phytoplankton cell division rates in the simulated Southern Ocean. *Global Biogeochemical Cycles*, *34*, e2019GB006380. https://doi.org/10.1029/2019GB006380

Received 29 JUL 2019
Accepted 16 MAR 2020
Accepted article online 4 APR 2020

Abstract We examine the effects of Southern Ocean eddies on phytoplankton cell division rates in a global, multiyear, eddy-resolving, 3-D ocean simulation of the Community Earth System Model. We first identify and track eddies in the simulation and validate their distribution and demographics against observed eddy trajectory characteristics. Next, we examine how simulated cyclones and anticyclones differentially modify iron, light, and ultimately population-specific cell division rates. We use an eddy-centric, depth-averaged framework to explicitly examine the dynamics of the phytoplankton population across the entire water column within an eddy. We find that population-averaged iron availability is elevated in anticyclones throughout the year. The dominant mechanism responsible for vertically transporting iron from depth in anticyclones is eddy-induced Ekman upwelling. During winter, in regions with deep climatological mixed layer depths, anticyclones also induce anomalously deep mixed layer depths, which further supply new iron from depth via an increased upward mixing flux. However, this additional contribution comes at the price of deteriorating light availability as biomass is distributed deeper in the water column. Therefore, even though population-averaged specific division rates are elevated in Southern Ocean anticyclones throughout most of the year, in the winter, severe light stress can dominate relieved iron stress and lead to depressed division rates in some anticyclones, particularly in the deep mixing South Pacific Antarctic Circumpolar Current. The opposite is true in cyclones, which exhibit a consistently symmetric physical and biogeochemical response relative to anticyclones.

1. Introduction

Observations (Doney et al., 2003; Frenger et al., 2018; Gaube et al., 2015; Large, 1998; McGillicuddy et al., 2007) and models (Anderson et al., 2011; Harrison et al., 2018; Song et al., 2018) agree that mesoscale activity helps regulate spatial and temporal variability in biological productivity and phytoplankton distributions (Doney et al., 2003; Glover et al., 2018). The Southern Ocean is replete with mesoscale activity (Meredith, 2016; Stevens & Killworth, 1992) and is a key regional contributor to the global "biological pump" (Hauck et al., 2015). However, recent work (i.e., Dawson et al., 2018; Frenger et al., 2018; Song et al., 2018) has emphasized that the biophysical relationship between Southern Ocean eddies and productivity is not fully understood. To better constrain Southern Ocean primary productivity, carbon storage (Marinov et al., 2008) and ultimately global climate dynamics (Chisholm, 2000), it is important to understand the degree to which eddies induce/stifle net primary production. To do so, the first step is to examine how cyclones and anticyclones differentially modify phytoplankton cell division rates. In the Southern Ocean, phytoplankton cell division rates are primarily controlled by light (Fauchereau et al., 2011) and iron (Boyd, 2002). Here, we use an eddy-centric framework, to explicitly examine how simulated eddies regulate light and iron limitation to drive anomalous division rates averaged across the entire depth-integrated phytoplankton population within them. The combined effect of anomalous division rates, loss rates, and physical transport on eddy-induced biomass anomalies is then considered in Rohr et al. (2020).

Several mechanisms are capable of modifying light and iron availability in Southern Ocean cyclones (supporting information Figure S1). In the vertical direction, eddy pumping caused by the upward deformation of isopycnals can lead to nutrient upwelling transiently during eddy intensification (Falkowski et al., 1991). Additionally, eddy-induced Ekman downwelling caused by the clockwise rotation of eddy-driven surface currents can lead to nutrient downwelling continuously throughout the lifetime of an eddy. (Dewar & Flierl, 1987; Gaube et al., 2014). Finally, increased stratification caused by domed isopycnals and cold temperature anomalies can lead to anomalously shallow mixed layer depths (Hausmann et al., 2017). For phytoplankton, anomalously shallow mixed layer depths are expected to decrease deep iron availability (Carranza & Gille, 2015) but increase population-averaged light availability (Nelson & Smith, 1991). Southern Ocean anticyclones, which rotate counterclockwise, depress isopycnals, and induce warm sea surface temperature anomalies ($SST' > 0$), are expected to induce the opposite response (downward eddy pumping, upward eddy-induced Ekman pumping, and anomalously deep mixed layer depths). Eddies can also induce biogeochemical anomalies by advecting tracers laterally via stirring (Chelton et al., 2011; Doney et al., 2003; Glover et al., 2018) and trapping (Early et al., 2011; Flierl, 1981; Lehahn et al., 2011); however, lateral processes are less likely than vertical processes to stimulate or depress new production and carbon export.

The existence of multiple pathways through which eddies can force a biological response (Gaube et al., 2014; McGillicuddy, 2016) makes it difficult to diagnose the precise cause of biogeochemical anomalies within them. Satellite observations have shown dramatic regional and seasonal variability in the correlation between sea surface height anomalies (SSH'—a proxy for eddies) and surface chlorophyll anomalies ($[Chl]_S'$—a proxy for biomass) (Gaube et al., 2013, 2015; Song et al., 2018). This variability implies that different mechanistic pathways can dominate at different times and locations (Gaube et al., 2014). Unfortunately, remote sensing studies are limited in their ability to assess depth-integrated population dynamics, biological rate terms, and many in situ biogeochemical processes (e.g., nutrient transport), often leaving uncertainty in the mechanisms driving observed correlative relationships. Frenger et al. (2018), for instance, observed that anticyclones in the Antarctic Circumpolar Current (ACC) are associated with elevated chlorophyll in the shallow mixing summer months and depressed chlorophyll in the deep mixing winter months but could not fully constrain the underlying drivers. Modeling work (Song et al., 2018) examining the relationships between SSH and $[Chl]_S$ anomalies in a general sense has gone on to propose that this seasonal flip hinges on the relative dominance of iron versus light limitation driven by changes in the climatological mixed layer depth but did not explicitly identify eddy structures or anomalous biological rates within them. To better understand if eddies are modifying new production or simply moving biomass around, this past work has underscored the need to leverage numerical simulations to directly address the effect of eddies on the entire biomass profile (Gaube et al., 2014), quantify the source and consequence of anomalous nutrient and light limitation (Song et al., 2018), and explicitly resolve biological rate terms (Frenger et al., 2018).

Here, we use the same global, multiyear, eddy-resolving, 3-D ocean simulation employed by Song et al. (2018) to explicitly examine how simulated eddies modify the phytoplankton division rates by regulating light and iron availability. First, we track individual eddies, identified as closed contours in SSH' (Faghmous et al., 2015), and compare these model-based eddy tracks to observations (section 3.1). After validating the simulated eddy tracks, we compute anomalies of physical and depth-averaged, biomass-weighted biogeochemical variables in a semi-Lagrangian, eddy-centric framework. We then provide a statistical analysis of these anomalies throughout the Southern Ocean and examine how they vary with eddy properties (e.g., polarity and size) and background environmental conditions (e.g., climatological mixed layer depth) (section 3.2). Next, we examine the anomalous vertical transport of iron to understand how eddies supply and suppress new iron to phytoplankton (section 3.3). Finally, we examine the intense seasonal variability in the South Pacific ACC pointed out by Frenger et al. (2018) and Song et al. (2018) to provide a step-by-step breakdown of the pathways by which eddy-modified light and iron can modify phytoplankton division rates in different ways (section 3.4). In the discussion, we compare simulated anomalous eddy-induced mixed layer depths (section 4.1), iron transport (section 4.2), and cell division rates (section 4.3) to theoretical and observational estimates in the literature.

2. Methods

2.1. Numerical Simulation

We analyze a global, eddy-resolving, numerical simulation integrated with the ocean (Smith et al., 2010), sea ice (Hunke & Lipscomb, 2008), and marine biogeochemistry (Moore et al., 2013) components of the the Community Earth System Model (CESM1) (Hurrell et al., 2013), forced with atmospheric data from the Coordinated Ocean-ice Reference Experiment (CORE I) "normal year" (Large & Yeager, 2004; Griffies et al., 2009). This simulation was run for 5 years after initialization (see Harrison et al., 2018, for details on spin-up/initialization), and model output was saved as 5-day means.

2.1.1. Physics

The physical ocean component is based on the Parallel Ocean Program version 2 (POP) (Smith et al., 2010) and was integrated on a global tripole grid with nominal horizontal spacing of 0.1° and 62 vertical levels. Vertical resolution is 10 m over the euphotic zone (0–150 m) and then decreases with depth. High spatial resolution permits mesoscale dynamics and the prognostic development of ocean eddies (Hallberg, 2013; Harrison et al., 2018; Song et al., 2018). Mesoscale variability compares well to AVISO satellite products and captures the intense variability observed in the Southern Ocean (Harrison et al., 2018). A validation of eddy demographics with observed eddy tracks is presented here in section 3.1.

Vertical mixing is based on the K-profile parameterization (KPP) developed by Large et al. (1994). The high-resolution integration employed here has been shown to capture deeper, more realistic winter mixed layers and improved spatial patterns throughout the Southern Ocean (Harrison et al., 2018) than coarser resolution CESM1 simulations that have underestimated deep winter mixing by 100s of meters in the Southern Ocean (Moore et al., 2013; Weijer et al., 2011). Note that while the KPP scheme is employed in both the high- and low-resolution simulations, it is sensitive to the changes to the mean flow and lateral mixing experienced in the high-resolution simulation. While biases still exist, the mean simulated climatological winter mixed layer depth is over 300 m across much of the ACC, particularly in the South Pacific and South Indian Oceans, which compares favorably with observations (Buongiorno Nardelli et al., 2017).

Sea ice is treated using the CICE4 component (Hunke & Lipscomb, 2008). The ice model does not sequester iron or simulate biogeochemistry. All atmospheric dust deposition over sea ice is deposited directly into the surface water.

2.1.2. Biogeochemistry

Biogeochemistry in the water column is treated with the Biogeochemical Element Cycle (BEC) model (Moore et al., 2013). Global solutions, integrated at a coarser resolution, have been widely validated against global data sets and shown to capture basin-scale spatial distributions in primary production, nutrient and chlorophyll concentrations (Doney et al., 2009, Moore et al., 2001, 2004, 2013), and key aspects of oceanic iron (Moore & Braucher, 2008) and carbon cycling (Lima et al., 2014; Long et al., 2013; Moore et al., 2013). More recently, this high resolution run has been shown to compare favorably to global chlorophyll distributions (Harrison et al., 2018) and match the observed Southern Ocean mesoscale variability in the correlation between $[Chl]'_S$ and SSH' (Song et al., 2018). Note that phytoplankton chlorophyll and carbon biomass have been shown to be well correlated in the observed Southern Ocean (Arrigo et al., 2008; Behrenfeld et al., 2005; Le Quéré et al., 2002).

BEC features a single class of zooplankton and three classes of phytoplankton: diatoms, small phytoplankton, and diazotrophs. Phytoplankton carbon biomass, C_{phyto} (mmol C), is resolved independently for each phytoplankton pool (*phyto*) and tracked in terms of grid cell concentration, $[C_{phyto}]$ $(\frac{\text{mmol C}}{\text{m}^3})$. Class-specific phytoplankton net population growth $(\frac{d[C_{phyto}]}{dt})$ is governed by a photosynthetic net primary productivity term, P_{phyto} $(\frac{\text{mmol C}}{\text{m}^3\text{d}})$ and opposed by a loss term, $Loss_{phyto}$ $(\frac{\text{mmol C}}{\text{m}^3\text{d}})$, such that

$$\frac{d[C_{phyto}]}{dt} = P_{phyto} - Loss_{phyto}. \tag{1}$$

$Loss_{phyto}$ is composed of nonlinear grazing, linear mortality, and quadratic mortality/aggregation terms.

P_{phyto} is equal to a volumetric specific photosynthetic division rate, $\mu_{phyto}(\text{d}^{-1})$, multiplied by the biomass concentration ($P_{phyto} = \mu_{phyto} * [C_{phyto}]$). This division rate is subject to temperature dependence (L^T), multinutrient (N, P, Si, Fe) limitation (L^N_{phyto}) and light availability ($L^{I_{par}}_{phyto}$) such that

$$\mu_{phyto} = \mu^{max}_{phyto} * L^T * L^N_{phyto} * L^{I_{par}}_{phyto}, \tag{2}$$

where μ^{max}_{phyto} is the maximum class-specific, mass-specific division rate. Unitless limitation terms vary from 0 to 1 and scale the maximum division rate such that lower values translate more limitation and reduced growth. The model and observations agree that Southern Ocean productivity is primarily limited by light (Fauchereau et al., 2011) and iron (Boyd, 2002), rather than temperature (L^T) or other nutrients. CESM1-BEC is able to reproduce large high nitrate low chlorophyll (HNLC) regions in the Southern Ocean, subarctic and equatorial Pacific (Harrison et al., 2018; Moore et al., 2004; Moore & Braucher, 2008). Regions of unutilized phosphate and nitrogen are pervasive throughout the simulated Southern Ocean, extending north of 40°S (see Figure 1 of Moore et al., 2004).

Light limitation is computed following a modified form of the growth model developed by Geider et al. (1998) and is functionally dependent on photosynthetically available radiation, the most constraining nutrient limitation term, and a dynamic *Chl*to*C* ratio. Class-specific nutrient limitation terms ($L^{Fe}_{phyto}, L^{P}_{phyto}, L^{N}_{phyto}, L^{Si}_{phyto}$) vary as a Holling-III nonlinear function of the available nutrient concentration and the class-specific half saturation coefficient. Multinutrient limitation is treated following Liebig's law of the minimum (van der Ploeg et al., 1999) such that the maximum specific division rate (μ^{max}_{phyto}) is only scaled by the most limiting nutrient limitation term. However, light and nutrient limitation are colimiting.

Iron is supplied to the ocean via atmospheric and benthic sedimentary sources following Moore and Braucher (2008). The physical transport of dissolved inorganic iron (Fe) is dominated by fluxes (μmol/m^2/d) from horizontal advection (U_{Fe}, V_{Fe}), vertical advection (W_{Fe}), and vertical diabatic mixing (Mix_{Fe}). All flux terms are averaged over the 5-day time step over which model output is saved. Vertical fluxes are positive in the upward direction.

2.2. Model Analysis

2.2.1. Biomass-Weighted, Depth-Averaged Variables

Throughout the Southern Ocean, surface biomass is not always well correlated with the depth-integrated biomass inventory (Rohr et al., 2017). Rather than focusing on surface concentrations (as done in Frenger et al., 2018; Gaube et al., 2014; Misumi et al., 2014; etc.), we express biogeochemically relevant variables as biomass-weighted, depth averages to capture the complete biological response to eddy perturbation. By representing the mean state of the entire phytoplankton population within an eddy, results are robust to variability in community composition, dilution during deep mixing (Behrenfeld et al., 2013; Rohr et al., 2017), biomass that may exist below a shallow mixed layer (Behrenfeld et al., 2013), and the possibility of nonuniform biomass profiles or subsurface maxima (McGillicuddy et al., 2007; Siegel et al., 1999). Biomass-weighted, depth averaged variables are identified with the subscript ($_\Sigma$) and are considered to be population-averaged (referring to the population within an eddy). They are computed as follows:

$$L^{Fe}_{\Sigma} = \sum_{k=0m}^{k=seafloor} \sum_{phyto=sp,diat} L^{Fe}_{k,phyto} \frac{[C_{phyto}]_k * h}{Biomass \quad Inventory}, \tag{3}$$

$$L^{I_{PAR}}_{\Sigma} = \sum_{k=0m}^{k=seafloor} \sum_{phyto=sp,diat} L^{I_{PAR}}_{k,phyto} \frac{[C_{phyto}]_k * h}{Biomass \quad Inventory}, \tag{4}$$

$$\mu_{\Sigma} = \sum_{k=0m}^{k=seafloor} \sum_{phyto=sp,diat} \mu_{k,phyto} \frac{[C_{phyto}]_k * h}{Biomass \quad Inventory}, \tag{5}$$

$$[Fe]_{\Sigma} = \sum_{k=0m}^{k=seafloor} \sum_{phyto=sp,diat} [Fe]_{k,phyto} \frac{[C_{phyto}]_k * h}{Biomass \quad Inventory}, \tag{6}$$

where $C_{phyto,k}$ is the class-specific biomass concentration at a given grid cell and depth ($\frac{\text{mmol C}}{\text{m}^3}$), h is the height of the grid cell (m), and the *BiomassInventory* is the depth-integrated sum of diatom and small phytoplankton biomass ($\frac{\text{mmol C}}{\text{m}^2}$). Note that only the two regionally dominant phytoplankton pools are considered, diatoms (*diat*) and small phytoplankton (*sp*). Iron concentrations only include the dissolved inorganic pool because it is the dominant form of iron and including other pools did not change the results.

Biomass-weighted, depth-averaged iron supply rates (μmol/m^3/d) capture the average rate at which iron is supplied to all phytoplankton across the water column by either vertical mixing or vertical advection. They are computed by averaging the vertical flux divergence at each grid cell over the water column and weighting by the fraction of the biomass inventory contained at each grid cell as follows:

$$\left.\frac{d[Fe]}{dt}\right|_{Mix,\ \Sigma} = \sum_{k=0m}^{k=seafloor} \sum_{phyto=sp,diat} (Mix_{Fe,bottom} - Mix_{Fe,top}) \frac{1}{h} \frac{[C_{phyto}]_k * h}{Biomass\quad Inventory} \tag{7}$$

$$\left.\frac{d[Fe]}{dt}\right|_{W,\ \Sigma} = \sum_{k=0m}^{k=seafloor} \sum_{phyto=sp,diat} (W_{Fe,bottom} - W_{Fe,top}) \frac{1}{h} \frac{[C_{phyto}]_k * h}{Biomass\quad Inventory}. \tag{8}$$

Iron supply rates are defined as positive if there is a net flux into the grid cell. This framework captures the degree that iron is transported to where phytoplankton actually are and ensures results are not biased by iron supplied to grid cells without any biomass. The total time-integrated supply of iron from either vertical mixing or advection is computed by integrating the supply rate between eddy formation and any given realization during its lifetime ($\int_{formation}^{realization} \left.\frac{d[Fe]}{dt}\right|_{Mix,\ \Sigma} dt$, etc).

2.2.2. Eddy-Induced Ekman Pumping

The velocity of eddy-induced Ekman pumping (cm/d) is estimated diagnostically from the curl of the relative surface stress ($\nabla \times \tau$) as follows:

$$\Omega_{Ek} = \frac{\nabla \times \tau}{\rho_o f}, \tag{9}$$

where τ is the relative surface stress between the wind and surface currents, ρ_o is the density of water, and f is the Coriolis parameter ($f = 2\Omega cos\theta$) at latitude θ with a global rotation rate Ω. Within simulated eddies, the curl of the relative surface stress and thus eddy-induced Ekman pumping is modified directly by rotating surface currents (Gaube et al., 2015; McGillicuddy, 2016). The contributions from SST' feedback (Chelton et al., 2004; O'Neill et al., 2010) and submesoscale nonlinear effects (Gaube et al., 2014) are not resolved but are not expected to qualitatively change the results.

2.3. Depth Extrapolation

Some model output is extrapolated at depth as storage limitations prevent saving the full-depth profiles of all prognostic tracers. In this simulation biomass ($[C_{phyto}]_z$), division rates ($\mu_{phyto,z}$), and limitation terms ($L^{Fe}_{phyto,z}$ and $L^{I_{par}}_{phyto,z}$) were archived to 150 m. Dissolved iron ($[Fe]_z$) and all component fluxes were saved to the ocean floor.

If the the mixed layer depth (MLD) is shallower than 150 m it is reasonable to assume that biomass below 150 m cannot access the euphotic depth (∼100 m) and is likely negligible. In turn, we assume biomass concentrations are zero below 150 m if $MLD < 150$ m. However, during the winter deep, mixing can penetrate well below 150 m. In order to diagnostically characterize biomass beneath what has been explicitly saved during deep mixing events ($MLD > 150$ m), all relevant profiles are linearly extrapolated to the base of the MLD and assumed to drop to zero immediately below the MLD. Southern Ocean observations support the approximation of a uniform biomass profiles across deep winter mixed layers (Uitz et al., 2006).

2.4. Anomaly and Climatology Fields

Anomaly fields for each relevant variable (var') are strictly spatial and are computed by removing the mean field ($\overline{var}$) from the raw field (var), such that

$$var' = var - \overline{var}. \tag{10}$$

Mean fields were created by smoothing the raw fields with a 2-D low-pass loess filter. Following Gaube et al. (2014), a half power cutoff of 20° in longitude and 10° in latitude was used to create the sea surface height anomaly (SSH'), and a 6°×6° filter was used for all biogeochemically relevant fields to best target mesoscale variability, such that anomalies should not be biased by regional climatological variability. Additional filters (notably a 20°×10° version for biogeochemical fields) were tested but did not qualitatively affect the nature of the results. Three-dimensional anomaly fields were computed independently at each depth.

The time-evolving background climatology fields ($\overline{var}_{Clim}$) were computed by averaging each year day of model output (saved as 5-day averages) across the 5 years of simulation. To help remove lingering mesoscale variability left from the relatively short model run, climatologies were smoothed with a 30-day moving average in time and a 6° × 6° loess filter in space. Filters were chosen carefully to retain large-scale seasonal and geographic variability. Normalized fields (var'') were computed by dividing anomaly fields by the corresponding climatology, such that

$$var'' = \frac{var'}{\overline{var}_{Clim}}. \tag{11}$$

2.5. Eddy Identification and Tracking

Unlike much of the prior correlative work (e.g., Gaube et al., 2014; Song et al., 2018) our eddy-centric approach specifically operates on coherent mesoscale structures rather than individual grid cells that may have a strong SSH' signal but are less likely to be enclosed by a rotating vortex. Here, eddies are identified as closed contours in the sea surface height anomaly (SSH') field independently at each time step using the parameter-less algorithm originally developed by Chelton et al. (2011) and adapted by Faghmous et al. (2015). Using closed contours in the SSH' field to isolate eddies reduces the probability of including spurious, nonrotating mesoscale features and helps isolate the mechanisms that are unique to actual eddies. Song et al. (2018), for instance, estimate that 33% of analyzed data are not enclosed by an SSH' contour at all.

Individual eddy realizations are identified at each time step as the outermost closed contour surrounding a single extremum. For cyclones, this extremum is a local minimum ($-SSH'$), and for anticyclones, it is a local maximum ($+SSH'$). The amplitude is defined as the difference between the extrema and outermost contour. The speed-based eddy radius (L_S) is approximated as the radius of a circle with an area equal to that enclosed by the SSH' contour around which the average geostrophic speed is maximized (Chelton et al., 2011). Eddy-averaged values were created for all relevant variables by colocating and averaging them across the footprint of each eddy realization.

After identification, eddy "realizations" are associated between time steps to create a portfolio of eddy tracks, each composed of a time series of eddy realizations. Eddy realizations at time step t are associated with the closest realization at time step $t+1$ within a predefined search radius, bounded by the maximum theoretical distance the eddy could have traveled between time t and $t+1$ (Faghmous et al., 2015). Once the closest realization has been identified at time $t+1$, it is checked to confirm both features are similar in size and amplitude. This process is iterated until no suitable eddy realization is found. Eddy tracks that last less than 60 days or never enter the Southern Ocean (south of 40°S) were not considered. The Weddell Sea region, where the simulation develops a large polynya with unrealistically deep mixed layer depths, was excluded from consideration. No further filtering was imposed unless explicitly mentioned.

In section 3.1 the distribution and demographics of simulated eddy tracks are compared to observed eddy tracks originally reported by Chelton et al. (2011) and more recently updated by Chelton and Schlax (2016) using improved altimeter observation described by Pujol et al. (2016) and a variation of the tracking methodology described by Williams et al. (2011).

2.6. Eddy Subsets

The Southern Ocean is defined from the pole to 40°S (e.g., Figures 1–3 and S2–S10). Eddies are said to be in the South Pacific (Figures 4–7) if they are found between 80°W < Lon < 180°W and are south of 40°S. Eddies are said to be in the ACC (Figures 7 and S11) if they are within the −20 cm and −80 cm SSH contours (Frenger et al., 2018), defined dynamically by the daily SSH climatology ($\overline{SSH}_{Clim}$). Eddies are referred to as large (small) if their radius is greater (less) than 50 km, and their SSH' amplitude is greater (less) than 5 cm. Eddies are referred to as deep (shallow) mixing if their background climatological mixed layer depth ($\overline{MLD}_{Clim}$) is deeper (shallower) than 100 m.

Eddy composite averages displayed in Figures 1–6 are averaged across all eddy realizations that fall within a given spatiotemporal bin. Composite anomalies are considered statistically significant if a one-sample t test rejects the null hypothesis that the sample set of eddy anomalies in a given bin comes from a normally distributed population with mean equal to zero at the 95% confidence level.

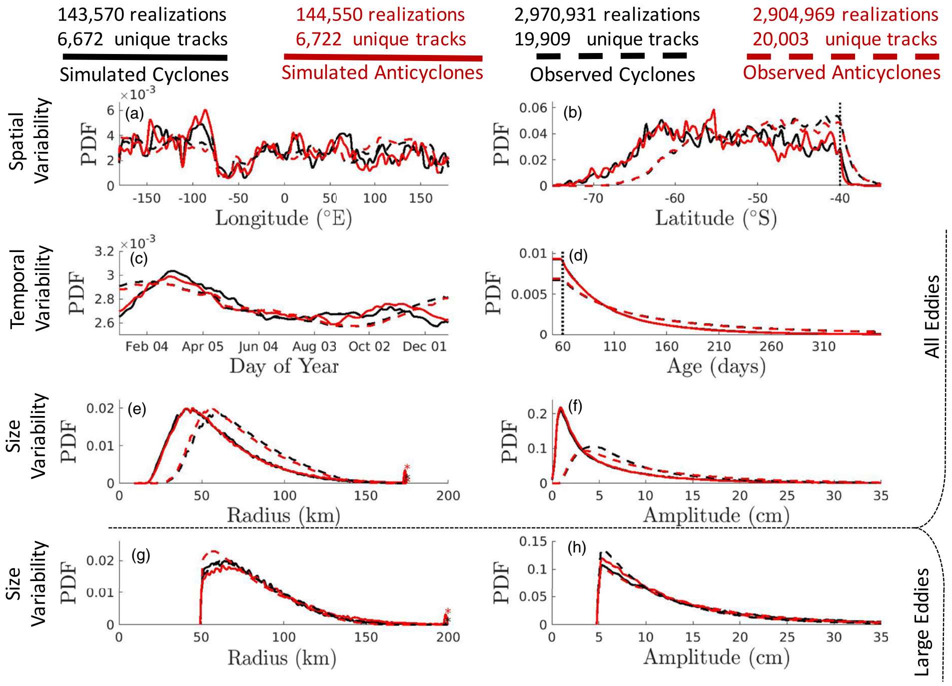

Figure 1. Simulated and observed eddy demographics. The probability distribution of all eddy realizations is plotted for various attributes of simulated cyclones (solid black) and anticyclones (solid red) alongside observed cyclones (dashed black) and anticyclones (dashed red). The entire set of Southern Ocean eddy realizations (see 2.6) is included in a–f. Vertical dashed lines indicate the constraints that eddy tracks must cross south of 40°S (b) and last at least 60 days (d). Note that eddies shorter than 60 days were removed from the observational tracks for a consistent comparison. Variability in the size of strictly large eddy realizations ($L_S > 50$ km; $Amplitude > 5$ cm), which comprise 35% of simulated realizations and 60% of observed realizations, is plotted in g–h.

3. Results

3.1. Simulated and Observed Eddy Track Demographics

A similar number of Southern Ocean eddies are identified in the simulated and observed eddy tracks each year. There are roughly 789 eddy realizations in the simulation and 708 in the observations during an average day. These realizations comprise 13,414 unique eddy tracks in the simulation (or 2,682 per year) and 39,912 tracks in the observational record (or 1,814 per year). Although there are fewer unique eddy tracks per year in the observations, observed eddies tend to last longer, with an average lifespan of 147 days compared to 109 days in simulated eddies.

Variability in the location, timing, and size of simulated and observed eddies are compared in Figure 1. The zonal distribution of eddies compares favorably between simulation and observation (Figure 1a); however, meridionally observations do not identify as many eddies at high latitudes as the simulation does (Figure 1b). Seasonally, eddies are more likely to occur in the summer in the observations than the simulation (Figure 1c). Observed eddies tend to be larger in radius (Figure 1e) and amplitude (Figure 1f) than simulated eddies. Filtering out simulated eddies beneath sea ice, features which cannot be observed from space, reduces the bias in the meridional distribution but does not remove the bias in eddy size. Note that simulated eddies south of 60°S, where the model identifies more eddies, tend to be much smaller ($\overline{L_S} = 45$ km; $\overline{Amplitude} = 4.2$cm) than those at lower latitudes ($\overline{L_S} = 66$ km; $\overline{Amplitude} = 7.5$cm) where the Rossby radius is much larger, likely accounting for the bias in small simulated eddies. The distribution of only large eddies is generally consistent between the simulation and observations (Figures 1g and 1h). For this reason, large eddies are often considered independently in our analysis (see section 2.6).

Both observed and simulated tracks were detected using similar geometrically based algorithms derived from Chelton et al. (2011) (see section 2.5); therefore, this comparison is unlikely to be biased by differences in detection methodology. Maps of the geographic distribution of simulated eddy tracks during each season are provided in Figure S2. Maps of the distributions of observed tracks can be found at https://wombat.coas.

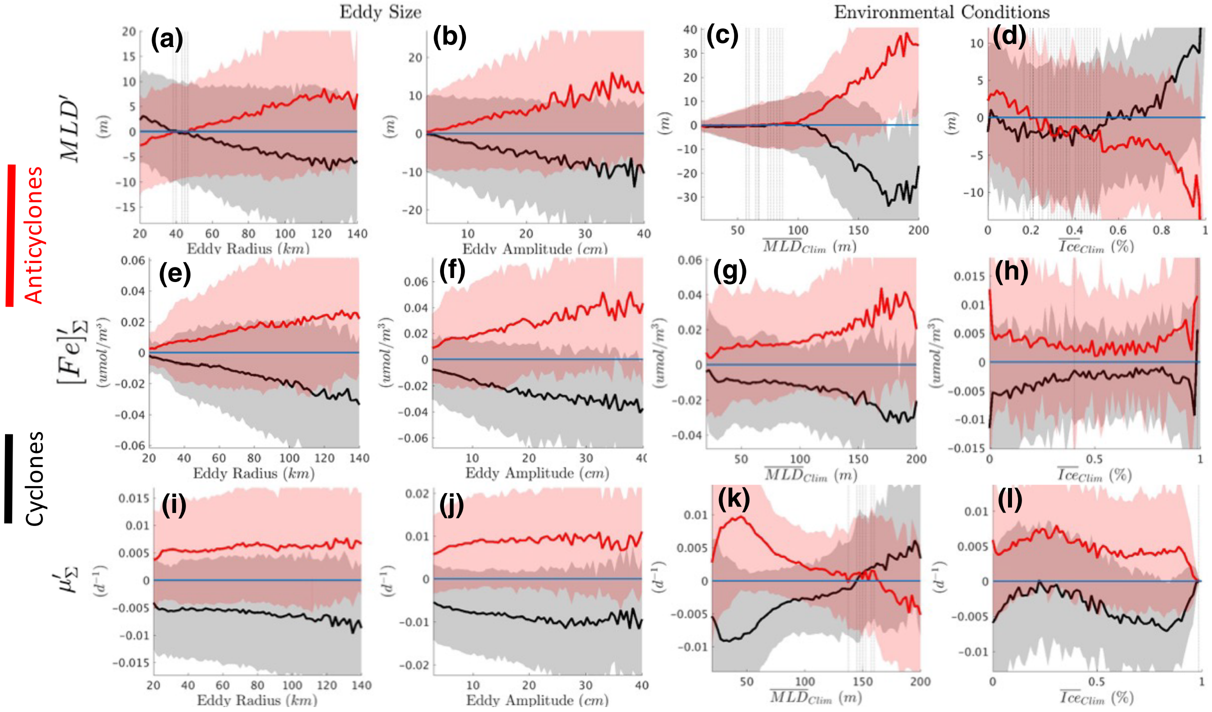

Figure 2. Variability in eddy anomalies. Variability in anomalous (a, b, c, d) mixed layer depths, (e, f, g, h) depth-integrated, biomass-weighted iron concentrations, and (i, j, k, l) depth-integrated, biomass-weighted division rates as a function of eddy radius (first column), eddy amplitude (second column), the climatological mixed layer depth (third column), and the climatological ice fraction (forth column). Cyclones are plotted in black. All Southern Ocean Eddies are included. Anticyclones are plotted in red. Error bars (shaded) denote +/− 1 standard deviation. Bins in which the difference between cyclones and anticyclones is statistically insignificant at the 95% confidence level are hatched out with vertical dotted lines.

oregonstate.edu/eddies/index.html (Chelton & Schlax, 2016). Simulated biomass distributions are included in Figures S2e–S2h to provide context for where simulated eddies travel relative to regions of high or low biomass.

3.2. Statistical Analysis of Anomalous Iron, Light, and Division Rates in Simulated Southern Ocean Eddies

Throughout the simulated Southern Ocean, biomass-weighted, depth-averaged cell division rates (μ_Σ) are widely depressed in cyclones and elevated in anticyclones (Table 1 and Figure S3). Average anomalies are 6.5% of colocated climatological values (Table 1; Figure S3) and driven by consistently modified iron limitation within eddies. However, in certain eddies, if the mixed layer is sufficiently deep, coincident modifications to light limitation can drive a reversal in the direction of anomalous division rates. Eddy-modified iron concentrations, mixed layer depths, and the competing effects of the associated iron and light limitation anomalies on division rates throughout the Southern Ocean are quantified in Table 1, plotted in Figures S3–S7, and described below.

On average, simulated cyclones increase biomass-weighted, depth-averaged iron limitation $(-L_\Sigma^{Fe'})$ by decreasing the iron concentration available to phytoplankton populations within them $(-[Fe]'_\Sigma)$, while anticyclones decrease iron limitation by increasing iron concentrations (Table 1; Figures S4 and S5). The magnitude of the anomalous iron concentration is on average greater than 10% of colocated climatological iron concentrations (Figure S4) and tends to increase with eddy size and the depth of the climatological mixed layer (Figures 2e–2g). The transport mechanisms by which this iron is supplied and suppressed in eddies are described in section 3.3.

Anomalous biomass-weighted, depth-averaged light limitation $(L_\Sigma^{I_{PAR}'})$ is controlled by eddy-induced changes to vertical mixing and, to a lesser extent, self-shading. Therefor, anomalous light limitation is anticorrelated with both the anomalous mixed layer depth $(r = -0.53)$, which increases light stress as the population is mixed into poorly-lit deep water, as well as the anomalous biomass inventory $(r = -0.29)$,

Table 1

Frequency and Magnitude of Eddy Anomalies

	Cyclones			Antiyclones		
	Large & Deep	All	Small & Shallow	Large & Deep	All	Small & Shallow
Realizations	9364(6.5%)	143570(100%)	44507(31%)	9910(6.9%)	144550(100%)	58086(40%)
Unique Tracks	1188(18%)	6672(100%)	5238(79%)	1179(17%)	6742(100%)	5282(78%)

Statistical distribution of eddy anomalies

Variables		$freq$	$mean$	$freq$	$mean$	$freq$	$mean$	$freq$	$mean$	$freq$	$mean$	$freq$	$mean$
MLD' (m)	+	28%	9.9(7.6)	50%	4.9(6.8)	57%	4.5(7.7)	78%	27(18)	51%	7.8(9.0)	42%	4.1(7.5)
	−	72%	-29(-16)	50%	-7.9(-8.6)	43%	-4.3(-7.7)	22%	-7.2(-5.6)	49%	-4.7(-6.8)	58%	-5.1(-8.3)
$L_{\Sigma}^{I_{PAR}'}$	+	80%	1.6e-2(11)	46%	9.1e-3(4.7)	34%	8.8e-3(4.7)	14%	5.2e-3(3.6)	51%	7.9e-3(4.2)	64%	9.9e-3(5.8)
	−	20%	-6.8e-3(-4.7)	54%	-7.8e-3(-4.2)	66%	-9.6e-3(-5.3)	86%	-1.6e-2(-10)	49%	-8.8e-3(-4.6)	36%	-7.7e-3(-4.0)
$[Fe'_{\Sigma}]$ $(\frac{\mu mol}{m^3})$	+	11%	4.4e-2(14)	27%	1.1e-2(8.4)	31%	7.2e-3(8.0)	91%	2.1e-2(14)	71%	1.4e-2(12)	66%	9.9e-3(11)
	−	89%	-1.9e-2(-11)	73%	-1.4e-2(-10)	69%	-9.4e-3(-9.2)	9%	-3.4e-2(-5.6)	28%	-1.1e-2(-7.7)	34%	-7.9e-3(-8.2)
$L_{\Sigma}^{Fe'}$	+	11%	1.6e-2(2.0)	26%	1.3e-2(2.1)	30%	1.4e-2(2.4)	92%	2.1e-2(2.8)	72%	1.9e-2(3.1)	68%	1.9e-2(3.3)
	−	89%	-2.0e-2(-2.7)	74%	-1.8e-2(-2.9)	70%	-1.8e-2(-3.1)	8%	-4.9e-3(-0.6)	28%	-1.2e-2(-2.2)-2.2	33%	-1.4e-2(-2.5)
μ'_{Σ} (d^{-1})	+	45%	8.1e-3(7.2)	22%	5.8e-3(5.0)	21%	5.0e-3(7.2)	51%	3.8e-3(4.4)	77%	8.7e-3(7.0)	78%	7.8e-3(8.2)
	−	55%	-4.3e-3(-4.5)	78%	-8.5e-3(-6.7)	79%	-7.7e-3(-8.4)	49%	-7.6e-3(-4.5)	23%	-5.4e-3(-6.4)	22%	-4.7e-3(-10)

Note. The percent of cyclones (left table) and anticyclones (right table) with positive or negative anomalies is reported along with the mean values of anomalies exclusively from eddies with a + or − anomaly. Anomalous mixed layer depth (MLD'), light limitation ($L_{\Sigma}^{I_{par'}}$), iron concentration ($[Fe]'_{\Sigma}$), iron limitation ($L_{\Sigma}^{Fe'}$), and division rates (μ'_{Σ}) are reported. In parenthesis the mean of the normalized anomalies, which is expressed as a percentage of the colocated climatology. Statistics are reported for all Southern Ocean eddies in addition to two subsets delineated based on size (large: $L_S >$ 50km and $Amplitude$ > 5cm; small: L_S < 50km and $Amplitude$ < 10cm) and background mixing (deep: $\overline{MLD}_{clim} > 100$ m; shallow: $\overline{MLD}_{clim} < 100$ m). The number (and %) of individual realization in each subset is provided above in addition to the number of unique eddy tracks that they come from. Note that not all realizations in a given track are represented in a particular subset.

which increases light stress as the population absorbs the ambient light. In small eddies with shallow climatological mixed layer depths ($\overline{MLD}_{Clim}$) the mixed layer depth anomaly (MLD') is typically inconsistent in direction and small in magnitude (< 5 m). In turn, the magnitude of anomalous light limitation is typically weak and dominated by self-shading rather than the dilution of the biomass profile. However, as both eddy size (Figures 2a and 2b) and the climatological mixed layer depth (Figure 2c) increase, so too does the magnitude of MLD' and the likelihood that it is in a direction that is consistent with the expected isopycnal deformation. In large eddies with deep climatological mixed layer depths, anomalous mixed layer depths are consistently shallow ($-MLD'$) in cyclones and deep ($+MLD'$) in anticyclones, with an average magnitude of nearly 30 m (Table 1). In turn, anomalous light limitation is well coupled to the anomalous mixed layer depth ($r = -0.87$) and on average over 10% larger than climatological values.

Variability in the size and direction of anomalous division rates is predominately associated with the climatological mixed layer depth (Figure 2k), which mediates the balance between the competing effects of eddy-modified light and iron limitation. When $\overline{MLD}_{Clim}$ is shallow, MLD' is small (Figure 2c), anomalous light limitation is not very relevant, and anomalous division rates are primarily modified by iron transported

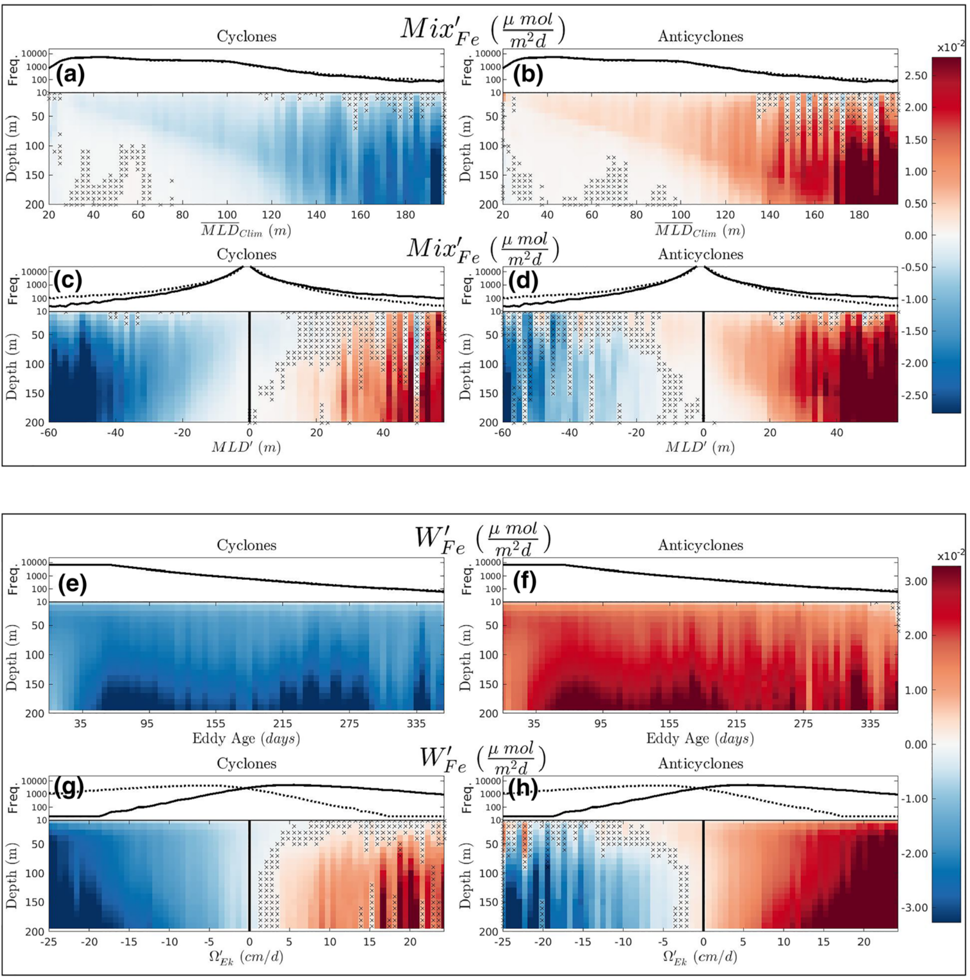

Figure 3. Vertical iron transport profiles for all Southern Ocean eddies. (a, b, c, d) Depth profiles of the anomalous vertical mixing flux of iron (Mix'_{Fe}) and (e, f, g, h) the anomalous vertical advection flux of iron (W'_{Fe}) averaged across all cyclones (left) and anticyclones (right). Mix'_{Fe} is plotted as a function of (a, b) the background climatological mixied layer depth ($\overline{MLD}_{Clim}$) and (c, d) the mixed layer depth anomaly (MLD'). W'_{Fe} is plotted as a function of (e, f) the eddy age and (c, d) the anomalous Ekman velocity (Ω'_{Ek}). Bins with anomalies that are statistically insignificant from 0 at the 95% confidence level are marked with an "*x*." The frequency of eddy realizations that fall on each bin on the *x*-axis is plotted above the corresponding profiles. Cyclonic (dashed lines) and anticyclonic (solid lines) distributions are included in each plot for ease of comparison.

via eddy-induced Ekman pumping (see section 3.3). As $\overline{MLD}_{Clim}$ and MLD' deepen, the magnitude of anomalous light limitation increases, damping the competing effect of anomalous iron limitation and reducing the magnitude of anomalous division rates. Eventually, the effect of eddy-modified light limitation exceeds that of iron limitation. Once $\overline{MLD}_{Clim}$ is deep enough (~ 150) m, μ'_{Σ} flips sign, with division rates more likely to be elevated in cyclones and depressed in anticyclones. In turn, seasonal variability in $\overline{MLD}_{Clim}$ can drive a seasonal reversal in the direction of μ'_{Σ}. This is clearly evident in the South Pacific ACC and discussed in detail in section 3.4.

3.3. Eddy-Induced Iron Transport

Eddy-modified mixed layer depths and eddy-induced Ekman pumping both preferentially enhance the vertical iron supply to phytoplankton inside of anticyclones and suppress it in cyclones (Figure 3) leading to consistently elevated and depressed iron concentrations in simulated Southern Ocean anticyclones and cyclones, respectively. The transient process of eddy pumping during formation acts in the opposite direction but does not appear to play a dominant role here. Together, the anomalous iron derived from vertical transport over the lifetime of an average eddy is on the order of 10% of background climatological levels, demonstrating that simulated eddies are capable of supplying or suppressing a meaningful contribution of iron from depth, thereby fueling or stifling new production. The role of each mechanism is described below for anticyclones; the opposite is true of cyclones.

Deeper mixed layers increase access to subsurface iron-rich water leading to an increase in the anomalous upward mixing flux of iron ($Mix_{Fe}^{'}$) in eddies with anomalously deep mixed layer depths, typical of large anticyclones. The magnitude and vertical penetration of this anomalous vertical mixing flux increase with the depth of the climatological mixed layer (Figure 3b) and the magnitude of the mixed layer depth anomaly (Figure 3d). Note that while some anticyclones do exhibit anomalously shallow mixed layer depths, these anticyclones are typically small and/or amidst shallow climatological mixed layers (see section 3.2), leading to a weak, inconsistent, and often statistically insignificant anomalous vertical mixing flux (left side of Figure 3d). In turn, the biomass-weighted, depth-averaged iron supply rate from vertical mixing ($\frac{d[Fe]}{dt}_{Mix,\ \Sigma}$) is elevated in the majority of anticyclones (68%), particularly in the ACC (81%) where *MLD* anomalies are very deep (Figure S6). However, the ensuing anomalous population-averaged iron concentration ($[Fe]'_{\Sigma}$) is not very well coupled to the anomalous mixed layer depth ($r = 0.14$) or the anomalous iron supply rate from vertical mixing ($r = 0.15$), particularly in regions with shallow climatological mixed layer depths (Figures 2c and 2g) and beneath heavy ice coverage (Figures 2d and 2h). In fact, the majority (71%) of anticyclones with anomalously shallow mixed layer depths still contain more iron ($+[Fe]'_{\Sigma}$) than the deeper mixing waters surrounding them. It is clear that another mechanism is also modifying the vertical iron profile and ultimately the population-averaged iron availability within eddies.

Eddy pumping does not explain the distribution of $[Fe]'_{\Sigma}$. If eddy pumping dominated, anticyclones would experience downwelling that depresses the upward advection of iron for a transient period during formation, followed by reduced iron concentrations. Instead, anticyclones predominately experience enhanced upward advection of iron ($+W_{Fe}^{'}$) that is maintained throughout their lifetimes (Figure 3f), coincident with elevated iron concentrations (Figure S4). A small contribution from eddy pumping may explain the slight reduction in the magnitude of W'_{Fe} apparent over the first month of eddy formation (Figure 3f) but is not large enough to change the sign of the anomaly.

Eddy-induced Ekman pumping, on the other hand, operates in a direction that is consistent with $W_{Fe}^{'}$ (Figure 3h) and appears to dominate the anomalous vertical advection of iron in eddies. Anomalous vertical velocities induced by rotating surface currents ($\Omega_{Ek}^{'}$) are upward in 88% of anticyclones (Figure S9). The size and direction of $\Omega_{Ek}^{'}$ are commensurate with anomalies in the total vertical velocity field (not shown), emphasizing the contribution of eddy-induced Ekman pumping to variability in vertical advection. As Ekman-induced vertical velocities increase, so too does the flux of iron via vertical advection (Figure 3h). Note that the small subset of anticyclones with anomalously downward eddy-induce Ekman pumping velocities (contradictory to their expected rotation) is associated with a less consistent and often statistically insignificant anomalous vertical advection flux (left side of Figure 3h). This likely has to do with the misidentification of mesoscale features as eddies that may not be rotating as a coherent vortex (i.e., meanders). Eddy-induced Ekman pumping appears to increase the rate at which vertical advection supplies iron to phytoplankton ($\frac{d[Fe]}{dt}_{W,\ \Sigma}$) in 75% of anticyclones and decrease it in 74% of cyclones (Figure S10).

Over the lifetime of an average simulated eddy realization, the time-integrated anomalous supply of iron from vertical advection is typically larger than the corresponding contribution from vertical mixing (Figure S11). Considering only large eddies in the ACC, vertical advection has supplied phytoplankton in the average anticyclone with 0.015 $\mu mol/m^3$ more iron since formation than in surrounding waters. Vertical mixing, on the other hand, only supplies an extra 0.005 $\mu mol/m^3$ of anomalous iron. However, the relative contribution of vertical mixing increases when exclusively considering the deepest mixing winter months or Pacific sector of the ACC. For context, vertical processes collectively modify iron concentrations by about 20% of background levels (~0.10 $\mu mol/m^3$), and because background concentrations are below the modelled half-saturation coefficient for diatoms (~0.15 $\mu mol/m^3$), the effect on iron limitation is more pronounced than in iron replete waters.

3.4. Seasonal Cycle of Anomalous Division Rates in the South Pacific ACC

Within South Pacific ACC eddies, seasonal variability in the relative size of competing iron and light limitation anomalies drives a reversal in the direction of division rates anomalies during the winter, consistent with the winter reversal in chlorophyll anomalies that has been observed (Frenger et al., 2018) and simulated (Song et al., 2018). Composite averaged annual cycles of the entire South Pacific (Figures 4–6) and

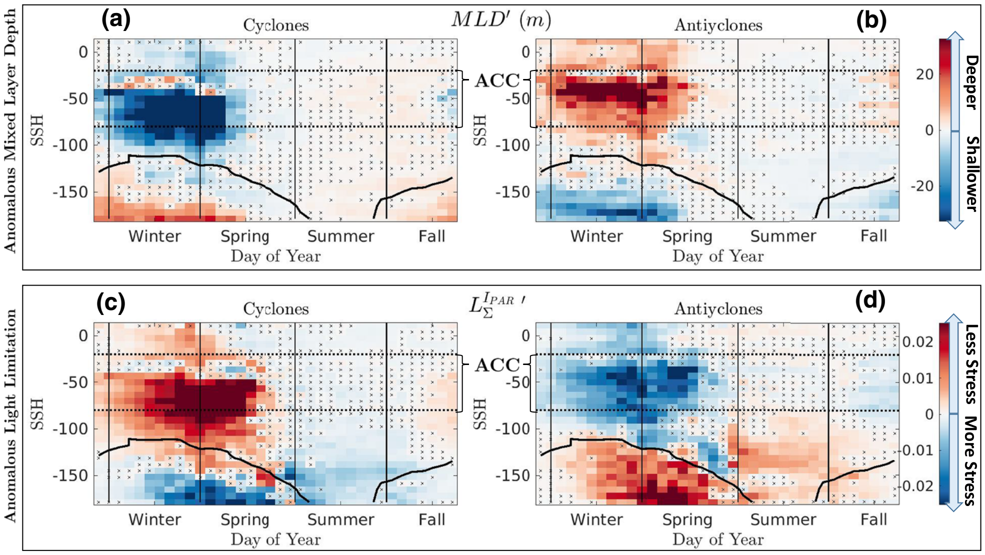

Figure 4. Composite averaged annual cycle of anomalous mixed layer depths and light limitation in South Pacific eddies. The anomalous (a, b) mixed layer depth (MLD') and (c, d) biomass-weighted, depth-averaged light limitation ($L_\Sigma^{I_{PAR}'}$) are plotted for cyclones (on the left) and anticyclones (on the right). Anomalies are plotted as a function of season and sea surface height (*SSH*). *SSH* serves as dynamic proxy for latitude to help align meanders in the *ACC* during zonal averaging. Only eddies in the Pacific sector (80°W < Lon < 180°W) of the Southern Ocean (Lat < 40°S) are included. The climatological ice edge (*Ice Fraction* > 80%) is overlaid with a solid black contour. The ACC is denoted with dashed horizontal lines. Anomalies are averaged across all eddy realizations that fall within a given bin, with the upper and lower 5% of values excluded. Bins that are not statistically significant from 0 at the 95% confidence level are denoted with a black **x**.

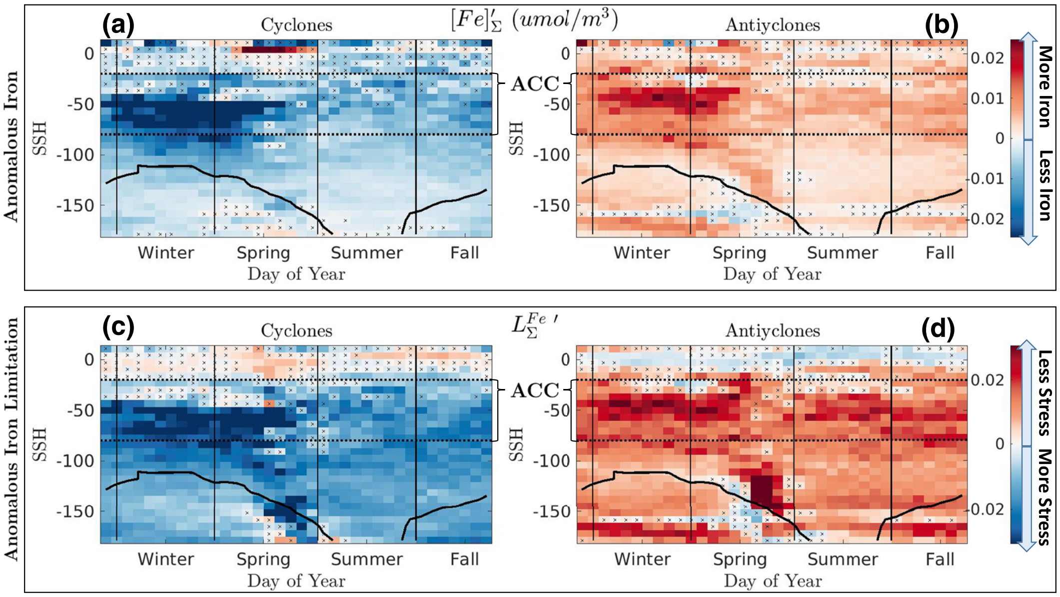

Figure 5. Composite averaged annual cycle of anomalous iron concentrations and iron limitation in South Pacific eddies. Identical to Figure 4 but for anomalous biomass-weighted, depth-averaged (a, b) iron ($[Fe]'_\Sigma$), and (c, d) iron limitation ($L_\Sigma^{Fe'}$).

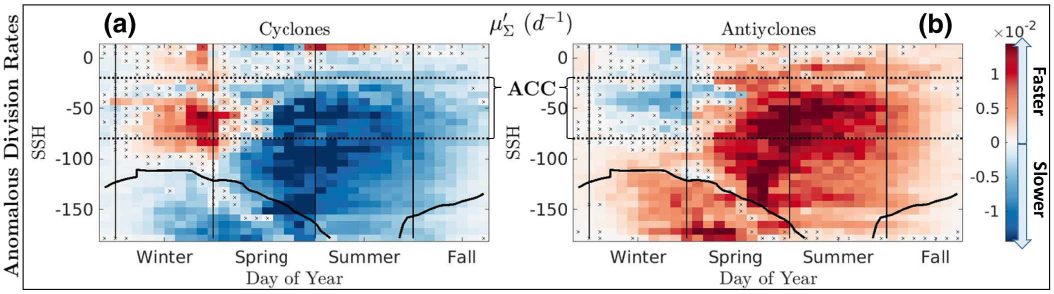

Figure 6. Composite averaged annual cycle of anomalous phytoplankton division rates in South Pacific eddies. Identical to Figure 4 but for (a, b) anomalous biomass-weighted, depth-averaged, population specific division rates (μ'_{Σ}).

depth resolved seasonal profiles of the isolated South Pacific ACC (Figure 7) illustrate, step by step step, how eddy-modified physical processes regulate this seasonal cycle in anomalous division rates. Below, these mechanistic pathways are described for anticyclones; the opposite is true in cyclones

In South Pacific anticyclones, the largest mixed layer depth anomalies (MLD') occur in the winter within the ACC, where background climatological mixing is deep (Figure 4b). Here the mixed layer depth in anticyclones is routinely 30 m deeper than surrounding waters. Biomass-weighted, depth-averaged light limitation ($L_{\Sigma}^{I_{PAR}\prime}$) is in turn exacerbated as the phytoplankton population is diluted across deeper, poorly lit, waters (Figures 4d and 7h). Exacerbated light limitation is sustained into early spring, after the mixed layer depth anomalies subside, through enhanced self-shading, driven by anomalously high concentrations of surface biomass associated with the spring bloom (Figure 7j; Rohr et al., 2020).

Anomalous iron concentrations ($[Fe]'_{\Sigma}$) are consistently elevated in anticyclones throughout the year but are strongest in the winter (Figure 5b). Anomalous iron is supplied seasonally by a strong vertical mixing flux driven by deep eddy-modified mixed layer depths during the winter (Figure 7b) and year-round by an eddy-modified vertical advective flux driven by eddy-induced Ekman pumping (Figure 7d). Biomass-weighted, depth-averaged iron limitation ($L_{\Sigma}^{Fe'}$) is in turn relieved throughout the year, especially in winter ACC eddies (Figures 5d and 7f).

Anomalous biomass-weighted, depth-averaged division rates (Figures 6b and 7l) are in turn driven by the combined effect of anomalous light (Figures 4d and 7h) and iron (Figures 5d and 7f) limitation. The role of iron dominates for much of the year, fueling anomalously high division rates, but the role of light dominates in the winter leading to anomalously low division rates. During the winter, relieved iron stress across the water column cannot compensate for the exacerbated light stress felt by the depth-integrated population as anomalously deep mixing redistributes the population into darker, deeper waters.

4. Discussion

4.1. Comparison of Theoretical, Simulated and Observed Mixed Layer Depth Anomalies

In nature, cyclones and anticyclones are expected to preferentially induce shallower and deeper mixed layers, respectively. However, this is not apparent in all simulated eddies (section 3.2). The eddies that are most likely to deform the mixed layer in a direction contradictory to their expected isopycnal deformation are often small (Figures 2a and 2b), amidst shallow background climatological mixed layers (Figure 2c), and/or below sea ice (Figure 2d). Numerically, it follows that smaller eddies with shallower mixed layers are not resolved as well as larger, deeper eddies. The magnitude of MLD' in these eddies is on average half the size (4.5 m) of the model's vertical resolution (10 m), and the size cutoff for the radius of “small” eddies (50 km) is only 5 times larger than the model's nominal horizontal resolution (10 km). From a physical perspective, anticyclones exhibiting shallow mixed layer depth anomalies may be partially explained by mode-water eddies, which dome the seasonal pycnocline but depress the main pycnocline, inducing a positive SSH anomaly like anticyclones but stratifying the surface ocean like cyclones (McGillicuddy et al., 2007, 2016); however, this does not explain why anomalously deep mixed layers depths appear in some cyclones. Finally, despite inconsistencies in direction, the magnitude of MLD' in these less energetic eddies is quite small, in agreement with observations of low magnitude anomalies in quiescent Southern Ocean eddies (Hausmann et al., 2017) and the theoretical physical underpinning that smaller eddies should not dramatically deform isopycnals.

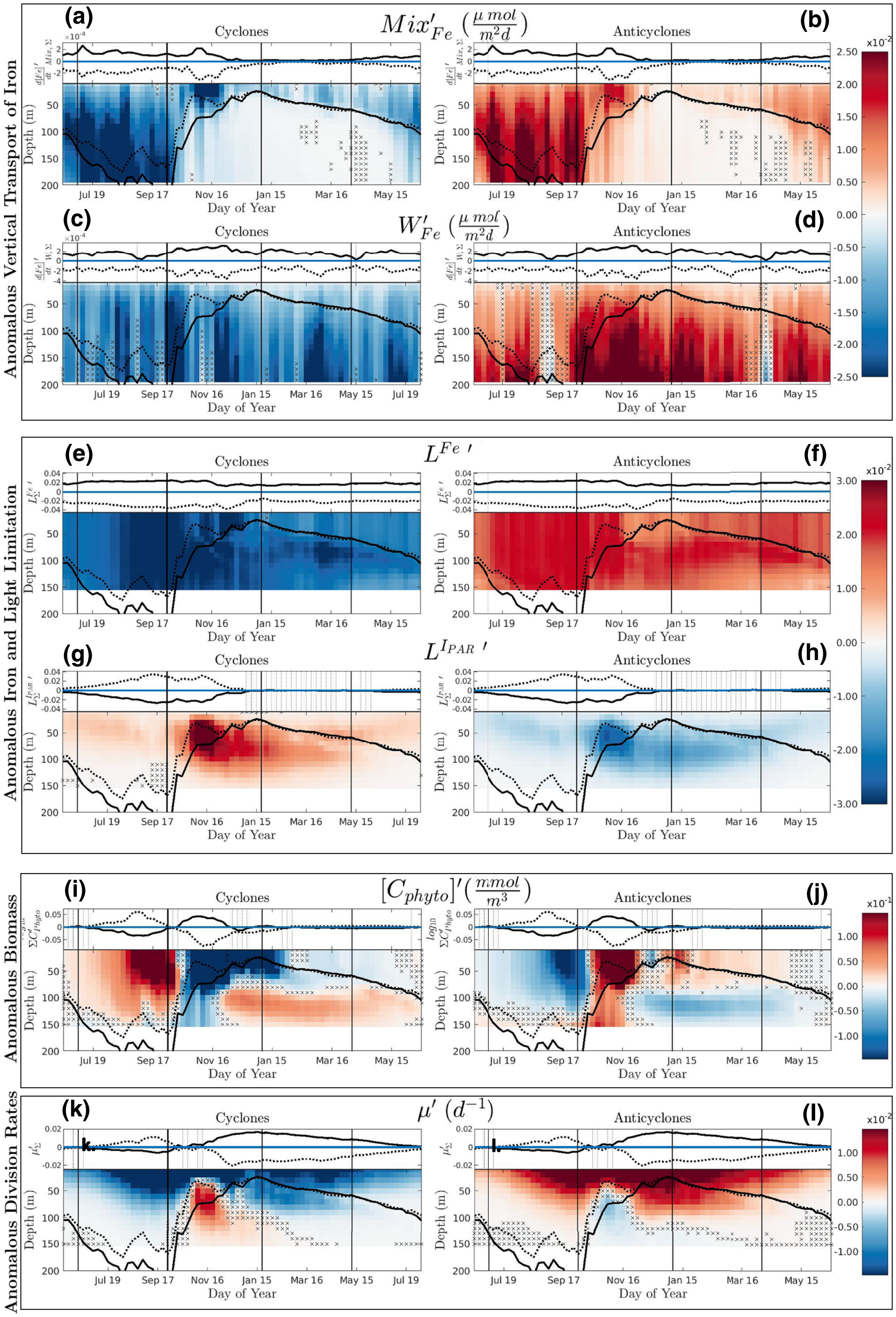

Figure 7. Composite averaged annual cycle of depth-resolved anomaly profiles in large South Pacific eddies within the ACC (see section 2.6). Qualifying eddy realizations that occur on the same day are binned together and averaged. In all, 9,087 realizations from 596 unique tracks are included. Profiles of seasonal variability in $L^{I_{PAR}\prime}$, $L^{Fe\prime}$, W'_{Fe}, Mix'_{Fe}, $[C_{phyto}]'$, and μ' are plotted for cyclones on the left and anticyclone on the right. The mean *MLD* in cyclones (dashed) and anticyclones (solid) is overlaid. Bins with anomalies that are statistically insignificant from 0 at the 95% confidence level are marked with an "*x*." Above each profile plot is a plot of the corresponding depth-averaged population mean. Bins in which the difference between cyclone and anticyclone anomalies are statistically insignificant at the 95% confidence level are marked with a dash vertical line. Solid vertical lines delineate seasons.

Eddies that are large or amidst deep climatological mixed layers do agree with theory (McGillicuddy, 2016) and observations (Hausmann et al., 2017). Peak MLD' is simulated and observed (Hausmann et al., 2017) to occur in the late winter along Southern Ocean current systems and increase with eddy amplitude. The magnitude of simulated anomalies (Figures 4 and S6 and Table 1) is smaller than observed, but this is largely because anomalies here are averaged over the entire lateral profile of eddies rather than just their core where MLD' is maximized (Hausmann et al., 2017). If only simulated eddy cores are considered (1/2 the eddy radius), then the magnitude of MLD' increases; peak anomalies are on average 59 m in the core of simulated, deep mixing, late winter anticyclones, compared to 60 m in observed late winter anticyclones within energetic Southern Ocean regions (Hausmann et al., 2017). However, the same subset of deep mixing, late winter cyclones have deeper mixed layer depths in the observations than the simulation due to larger mixed layer depth anomalies in the simulation; simulated cyclones exhibits anomalies of −63 m, rather than the less extreme −30 m found in the observations. It is unclear why the model does not reproduce this asymmetry in the magnitude of MLD', but it is unlikely that the qualitative balance of light and iron modification in cyclones is fundamentally biased.

4.2. Comparison of Theoretical, Simulated and Observed Iron Transport

Historically, observations have often attributed eddy-induced chlorophyll anomalies to eddy pumping during formation (Falkowski et al., 1991; McGillicuddy et al., 1998; Siegel et al., 1999). However, more recent work has identified substantial regional variability in the role of eddy pumping (Gaube et al., 2014, 2015) and highlighted the importance of eddy-induced Ekman pumping (Gaube & McGillicuddy, 2017; McGillicuddy et al., 2007; Zhang et al., 2018). The magnitude of simulated vertical velocities associated with eddy-induced Ekman pumping in the Southern Ocean is on average 16 cm/d but exceeds 67 cm/d in the strongest 5% of eddies. Note that this simulation does not resolve nonlinear submesoscale processes that could induce upwelling on the periphery of an eddy (Brannigan, 2016; Mahadevan et al., 2008). Nevertheless, simulated eddy-induced Ekman pumping velocities are in line with a globally observed mean of roughly 10 cm/d (Gaube et al., 2015) and an upper bound on the order of 100 cm/d (Martin & Richards, 2001). Although observed vertical velocities induced by eddy-pumping in the open ocean can reach 100 cm/d (Gaube et al., 2015; Siegel et al., 1999), they quickly subside after formation. It is not surprising, then, that continuous eddy-induced Ekman pumping can dominate the anomalous vertical advection of iron, particularly in the Southern Ocean where wind speeds are strong.

More surprising is the relative contribution of iron from the vertical mixing flux. The amplified role of eddy-induced Ekman pumping relative to mixed layer modification agrees with work by Zhang et al. (2018), who conclude that the vertical nutrient supply in Gulf Stream eddies is dominated by eddy-induced Ekman pumping rather than changes in vertical turbulent diffusion but contradicts Song et al. (2018) who conclude mixed layer depth anomalies are the dominant driver of eddy-induced iron fluxes. Song et al. (2018) came to this conclusion using an identical model integration to ours but computed the iron budget exclusively over the bulk mixed layer, not considering the distribution of the biomass profile which is not necessarily homogeneously distributed across the mixed layer (Carranza et al., 2018). This is an important distinction in the spring and summer because biomass can exist well below the mixed layer depth where it continues to be fed by eddy-induced Ekman pumping (Figures 7c and 7d) but is left out of the Song et al. (2018) budget. Further, a third of the Song et al. (2018) domain is not associated with coherent eddies (see section 2.5), so will not be subject to eddy-induced Ekman pumping.

Nevertheless, our results should not diminish the importance of the mixed layer depth modification. For instance, wintertime eddies with deep mixed layer anomalies ($MLD' > +10$ m) exhibit iron anomalies 350% larger on average than those in eddies with shallow mixed layer anomalies ($MLD' < -10$ m), which is qualitatively consistent with findings by Dufois et al. (2016) that deeper winter mixing in subtropical anticyclones increases productivity relative to cyclones. Instead, we want to caution that the anomalous iron supply from mixed layer modification is limited seasonally to the winter and regionally to deep mixing environments like the ACC. However, eddy-induced Ekman pumping appears to modify the iron supply with much more seasonal and regional consistency, particularly in the Southern Ocean where wind speeds are generally faster than subtropical gyres. Finally, it is important to remember that both mechanisms modify the vertical iron profile and are thus not independent. For instance, after the mixed layer shoals, eddy-induced Ekman pumping in anticyclones can continue to advect iron that was previously mixed up higher in the water column. This is consistent with the hypothesis proposed by Song et al. (2018) that winter preconditioning leaves some remnant of unused iron available to summer anticyclones. Eddy-induced Ekman pumping provides a mechanistic explanation of how this iron can be accessed after detrainment below a shoaling mixed layer.

By increasing local background vertical iron transport rates by 5–20%, it is possible that eddy-induced nutrient fluxes could help close the global nutrient budget for the upper ocean (Doddridge & Marshall, 2018; McGillicuddy et al., 2003); however, due to the symmetry between cyclones and anticyclones, much of this effect is cancelled out across the Southern Ocean. Averaged across all Southern Ocean cyclones and anticyclones, eddies do act as a net source of iron to phytoplankton, but the magnitude of that source drops to roughly 1% of background rates (4.7×10^{-5} mmol/m^3/d^1). The rectified iron supply does not average out completely because of the shape of the iron profile, which increases with depth, allowing anticyclones, which act deeper in the water column, to transport more iron up than cyclones can suppress. The net iron supply is likely underestimated by this simulation which does not resolve the observed asymmetry between the size of mixed layer depth anomalies in cyclones and anticyclones (Section 4.1; Figures 5a, 5b, and S6). If the magnitude of negative mixed layer depth anomalies in simulated cyclones was smaller (as observed), then deeper cyclonic mixed layer depths would lead to less cyclonic iron suppression and a larger rectified supply of iron, particularly in winter. Together, these vertical pathways for iron transport provide a plausible mechanism for a rectified source of new iron in Southern Ocean eddies but must be considered carefully in the context basin-scale cancellation and nonlinear Ekman pumping (Mahadevan et al., 2008) that is not resolved in this simulation.

Note that we focus on vertical nutrient pathways as these can supply or suppress new nutrients capable of stimulating or stifling new production but caution that anomalous iron concentrations are also influenced by lateral transport mechanisms. To confirm that anomalous vertical iron transport is not dwarfed by the horizontal advection of iron, we conservatively estimated the potential for anomalies to arise exclusively from lateral stirring or trapping by looking at the size and direction of the lateral iron gradient that horizontal transport mechanisms operate on. We estimated the stirring and trapping potential of each eddy following Frenger et al. (2018) and found that the supply of anomalous iron from horizontal mechanisms is similar in magnitude to that from vertical ones, suggesting that at least half of the iron anomaly in simulated eddies reflects the supply or suppression of new iron from depth. The distribution of anomalous iron supplied by vertical and lateral mechanisms in large, ACC eddies is included in Figure S11.

4.3. Comparison of Theoretical, Simulated, and Observed Anomalous Division Rates

We can confirm that simulated Southern Ocean eddies explicitly modify the division rates of the phytoplankton populations within them as inferred by past studies from chlorophyll anomalies (e.g., Frenger et al., 2018), correlative relationships (e.g., Gaube et al., 2015), and simulated shifts in light and iron availability (e.g., Song et al., 2018). Our results clearly demonstrate a consistent, population-averaged response; divisions rates are, on average, elevated in anticyclones and depressed in cyclones. This is implicitly consistent with observations (Frenger et al., 2018) and simulations (Song et al., 2018) of elevated and depressed $[Chl]_S$ inside of anticyclones and cyclones, respectively as well as recent observations of reduced productivity in a Southern Ocean cyclone (Ellwood et al., 2020). Overall, simulated division rates are ever so slightly more likely to be suppressed in any given eddy; 50.4% of all Southern Ocean eddies (cyclones and anticyclones) exhibit suppressed divisions rates (Table 1). However, note that Phaeocystis, which are prevalent in the Southern Ocean (Arrigo et al., 1998), do well under low light (Tang et al., 2009), and have a low iron-uptake efficiency (Schoemann et al., 2005) are not resolved. Including Phaeocystis would likely further amplify simulated population-averaged division rates in anticyclones, where mixing is deep, light is low, and iron is elevated. Further investigation into the simultaneous effects of dilution (Behrenfeld, 2010), grazing (Le Quéré et al., 2016), and lateral advection (Frenger et al., 2018) is warranted to confirm that variability in depth-averaged division rates is the dominant driver of variability in surface chlorophyll concentrations and net primary production.

Moreover, our results demonstrate that anomalous division rates in eddies can deviate from the mean and why they do so, helping corroborate the hypothesis that different mechanisms can dominate the biogeochemical response to eddy perturbation (Gaube et al., 2014). Specifically, observations (Frenger et al., 2018) and simulations (Song et al., 2018) have identified a seasonal flip in the direction of $[Chl]'_S$ along the ACC. Frenger et al. (2018) find that this reversal cannot be explained by quantitative estimates of lateral stirring or trapping and infer that variability in $[Chl]'_S$ must be driven by biological rate-based mechanisms. Song et al. (2018) go on to show that this seasonal variability is replicated in this simulation and associated with a corresponding shift in the dominance of light versus iron limitation. Here we go a step further and confirm that this shift is, in fact, manifest in μ'_{Σ} and is mechanistically consistent with increasing light limitation observed during deep mixing events in the Southern Ocean (Boyd, 2002; Fauchereau et al., 2011; Moore & Abbott, 2002; Venables & Meredith, 2009).

5. Conclusions

Our findings demonstrate the comprehensive manner by which simulated eddies modify the cell division rates of phytoplankton populations within them by modifying light and iron availability. Throughout the Southern Ocean, simulated cyclones and anticyclones induce a largely symmetric physical and biogeochemical response (i.e., similar magnitude and opposite direction). In anticyclones, eddy-induced Ekman pumping, driven by strong Southern Ocean winds and the counterclockwise rotation of their surface currents, consistently stimulates the upward advection of iron and elevates population-averaged iron availability. Deep mixed layer depth anomalies are found in large anticyclones with deep background mixing, such as those in the winter ACC, and provide additional iron to phytoplankton via an increased upward mixing flux. However, this extra iron comes at the price of increasing light stress, stymieing the ability of iron to elevate population-averaged division rates. The opposite is true in cyclones. The net effect is that population-averaged division rates are widely elevated in anticyclones and depressed in cyclones, but the magnitude of these anomalies is closely tied to the depth of the background climatological mixed layer. If the background climatological mixed layer is deep enough, the exacerbated (relieved) light limitation can dominate relieved (exacerbated) iron limitation and cause the direction of anomalous division rates to reverse in anticyclones (cyclones). This is most evident in the deep winter mixing South Pacific sector of the ACC.

Acknowledgments
The CESM project is supported by the National Science Foundation and the Office of Science (BER) of the U.S. Department of Energy. Computing resources were provided by the Climate Simulation Laboratory at NCAR's Computational and Information Systems Laboratory (CISL), sponsored by the National Science Foundation and other agencies. This research was enabled by CISL compute and storage resources. T. R. and S. C. D. acknowledge support from the National Aeronautics and Space Administration Ocean Biology and Biogeochemistry Program (NNX14AL86G) and the National Science Foundation Polar Programs award 1440435 (Antarctic Integrated System Science) to the Palmer LTER program. P. G. acknowledges support from the National Aeronautics and Space Administration Physical Oceanography Program (NNX16AH9G). Complete observational eddy tracks are available at http://wombat.coas.oregonstate.edu/eddies/index.html. The code used to track eddies in the model domain can be found at https://github.com/jfaghm/OceanEddies with detailed information publically available on sdata: https://doi.org/10.1038/sdata.2015.28. Complete simulated eddy tracks, along with the complete catalogue of environmental variables and anomalies within these eddies, are available in a .mat data structure at osf.io/cw7qt, https://doi.org/10.17605/OSF.IO/CW7QT. The primary scripts used to filter, plot, and analyze this data, in addition to extensive metadata information, can also be found at osf.io/cw7qt, https://doi.org/10.17605/OSF.IO/CW7QT.

References

Anderson, L. A., McGillicuddy, D. J., Maltrud, M. E., Lima, I. D., & Doney, S. C. (2011). Impact of eddy-wind interaction on eddy demographics and phytoplankton community structure in a model of the North Atlantic Ocean. *Dynamics of Atmospheres and Oceans*, *52*(1), 80–94. https://doi.org/10.1016/j.dynatmoce.2011.01.003

Arrigo, K. R., Robinson, D. H., Worthen, D. L., Schieber, B., & Lizotte, M. P. (1998). Bio-optical properties of the southwestern Ross Sea. *Journal of Geophysical Research*, *103*(C10), 21,683–21,695 en. https://doi.org/10.1029/98JC02157

Arrigo, K. R., van Dijken, G. L., & Bushinsky, S. (2008). Primary production in the Southern Ocean, 1997–2006. *Journal of Geophysical Research*, *113*, C08004 en. https://doi.org/10.1029/2007JC004551

Behrenfeld, M. J. (2010). Abandoning Sverdrup's critical depth hypothesis on phytoplankton blooms. *Ecology*, *91*(4), 977–989. https://doi.org/10.1890/09-1207.1

Behrenfeld, M. J., Boss, E., Siegel, D. A., & Shea, D. M. (2005). Carbon-based ocean productivity and phytoplankton physiology from space. *Global Biogeochemical Cycles*, *19*, GB1006. https://doi.org/10.1029/2004GB002299

Behrenfeld, M. J., Doney, S. C., Lima, I. D., Boss, E. S., & Siegel, D. A. (2013). Annual cycles of ecological disturbance and recovery underlying the subarctic Atlantic spring plankton bloom. *Global Biogeochemical Cycles*, *27*, 526–540. https://doi.org/10.1002/gbc.20050

Boyd, P. W. (2002). Environmental factors controlling phytoplankton processes in the Southern Ocean. *Journal of Phycology*, *38*(5), 844–861. https://doi.org/10.1046/j.1529-8817.2002.t01-1-01203.x

Brannigan, L. (2016). Intense submesoscale upwelling in anticyclonic eddies. *Geophysical Research Letters*, *43*, 3360–3369. https://doi.org/10.1002/2016GL067926

Buongiorno Nardelli, B., Guinehut, S., Verbrugge, N., Cotroneo, Y., Zambianchi, E., & Iudicone, D. (2017). Southern Ocean mixed-layer seasonal and interannual variations from combined satellite and in situ data: Southern Ocean mixed-layer variability. *Journal of Geophysical Research: Oceans*, *122*, 10,042–10,060. https://doi.org/10.1002/2017JC013314

Carranza, M. M., & Gille, S. T. (2015). Southern Ocean wind-driven entrainment enhances satellite chlorophyll-a through the summer. *Journal of Geophysical Research: Oceans*, *120*, 304–323. https://doi.org/10.1002/2014JC010203

Carranza, M. M., Gille, S. T., Franks, P. J. S., Johnson, K. S., Pinkel, R., & Girton, J. B. (2018). When mixed layers are not mixed. Storm-driven mixing and bio-optical vertical gradients in mixed layers of the Southern Ocean. *Journal of Geophysical Research: Oceans*, *123*, 7264–7289. https://doi.org/10.1029/2018JC014416

Chelton, D. B., Gaube, P., Schlax, M. G., Early, J. J., & Samelson, R. M. (2011). The influence of nonlinear mesoscale eddies on near-surface oceanic chlorophyll. *Science*, *334*(6054), 328–332. https://doi.org/10.1126/science.1208897

Chelton, D. B., & Schlax, M. G. (2016). Mesoscale eddies in altimeter observations of SSH: Oregon State University.

Chelton, D. B., Schlax, M. G., Freilich, M. H., & Milliff, R. F. (2004). Satellite measurements reveal persistent small-scale features in ocean winds. *Science*, *303*, 978–983. https://doi.org/10.1126/science.1091901

Chelton, D. B., Schlax, M. G., & Samelson, R. M. (2011). Global observations of nonlinear mesoscale eddies. *Progress in Oceanography*, *91*(2), 167–216. https://doi.org/10.1016/j.pocean.2011.01.002

Chisholm, S. W. (2000). Oceanography: stirring times in the Southern Ocean. *Nature*, *407*(6805), 685 En. https://doi.org/10.1038/35037696

Dawson, H. R. S., Strutton, P. G., & Gaube, P. (2018). The unusual surface chlorophyll signatures of Southern Ocean eddies. *Journal of Geophysical Research: Oceans*, *123*, 6053–6069. https://doi.org/10.1029/2017JC013628

Dewar, W. K., & Flierl, G. R. (1987). Some effects of the wind on rings. *Journal of Physical Oceanography*, *17*(10), 1653–1667. https://doi.org/10.1175/1520-0485(1987)017<1653:SEOTWO>2.0.CO;2

Doddridge, E. W., & Marshall, D. P. (2018). Implications of eddy cancellation for nutrient distribution within subtropical gyres. *Journal of Geophysical Research: Oceans*, *123*, 6720–6735. https://doi.org/10.1029/2018JC013842

Doney, S. C., Glover, D. M., McCue, S. J., & Fuentes, M. (2003). Mesoscale variability of sea-viewing wide field-of-view sensor (SeaWiFS) satellite ocean color: Global patterns and spatial scales. *Journal of Geophysical Research*, *108*(C2), 3024. https://doi.org/10.1029/2001JC000843

Doney, S. C., Lima, I., Moore, J. K., Lindsay, K., Behrenfeld, M. J., Westberry, T. K., et al. (2009). Skill metrics for confronting global upper ocean ecosystem-biogeochemistry models against field and remote sensing data. *Journal of Marine Systems*, *76*(1), 95–112. https://doi.org/10.1016/j.jmarsys.2008.05.015

Dufois, F., Hardman-Mountford, N. J., Greenwood, J., Richardson, A. J., Feng, M., & Matear, R. J. (2016). Anticyclonic eddies are more productive than cyclonic eddies in subtropical gyres because of winter mixing. *Science Advances*, *2*(5), e1600282. https://doi.org/10.1126/sciadv.1600282

Early, J. J., Samelson, R. M., & Chelton, D. B. (2011). The evolution and propagation of quasigeostrophic ocean eddies. *Journal of Physical Oceanography*, *41*(8), 1535–1555. https://doi.org/10.1175/2011JPO4601.1

Ellwood, M. J., Strzepek, R. F., Strutton, P. G., Trull, T. W., Fourquez, M., & Boyd, P. W. (2020). Distinct iron cycling in a Southern Ocean eddy. *Nature Communications*, *11*(1), 1–8. https://doi.org/10.1038/s41467-020-14464-0

Faghmous, J. H., Frenger, I., Yao, Y., Warmka, R., Lindell, A., & Kumar, V. (2015). A daily global mesoscale ocean eddy dataset from satellite altimetry. *Scientific data*, *2*, 150,028 English (US). https://doi.org/10.1038/sdata.2015.28

Falkowski, P. G., Ziemann, D., Kolber, Z., & Bienfang, P. K. (1991). Role of eddy pumping in enhancing primary production in the ocean. *Nature*, *352*(6330), 55. https://doi.org/10.1038/352055a0

Fauchereau, N., Tagliabue, A., Bopp, L., & Monteiro, PedroM. S. (2011). The response of phytoplankton biomass to transient mixing events in the Southern Ocean. *Geophysical Research Letters*, *38*, L17601. https://doi.org/10.1029/2011GL048498

Flierl, G. R. (1981). Particle motions in large-amplitude wave fields. *Geophysical & Astrophysical Fluid Dynamics*, *18*(1-2), 39–74. https://doi.org/10.1080/03091928108208773

Frenger, I., Münnich, M., & Gruber, N. (2018). Imprint of Southern Ocean mesoscale eddies on chlorophyl. *Biogeosciences*, *15*, 4781–4798. https://doi.org/10.5194/bg-2018-70

Gaube, P., Chelton, D. B., Samelson, R. M., Schlax, M. G., & O'Neill, L. W. (2015). Satellite observations of mesoscale eddy-induced Ekman pumping. https://doi.org/10.1175/JPO-D-14-0032.1

Gaube, P., Chelton, D. B., Strutton, P. G., & Behrenfeld, M. J. (2013). Satellite observations of chlorophyll, phytoplankton biomass, and Ekman pumping in nonlinear mesoscale eddies. *Journal of Geophysical Research: Oceans*, *118*, 6349–6370. https://doi.org/10.1002/2013JC009027

Gaube, P., & McGillicuddy, D. J. (2017). The influence of Gulf Stream eddies and meanders on near-surface chlorophyll. *Deep Sea Research Part I: Oceanographic Research Papers*, *122*, 1–16. https://doi.org/10.1016/j.dsr.2017.02.006

Gaube, P., Mcgillicuddy, D., Chelton, D. B., Behrenfeld, M. J., & Strutton, P. G. (2014). Regional variations in the influence of mesoscale eddies on near-surface chlorophyll. *Journal of Geophysical Research: Oceans*, *119*, 8195–8220. https://doi.org/10.1002/2014JC010111

Geider, R., Macintyre, H., & Kana, T. (1998). A dynamic regulatory model of phytoplanktonic acclimation to light, nutrients, and temperature. *Limnology and Oceanography - LIMNOL OCEANOGR*, *43*, 679–694. https://doi.org/10.4319/lo.1998.43.4.0679

Glover, D. M., Doney, S. C., Oestreich, W. K., & Tullo, A. W. (2018). Geostatistical analysis of mesoscale spatial variability and error in SeaWiFS and MODIS/Aqua Global Ocean Color Data. *Journal of Geophysical Research: Oceans*, *123*, 22–39. https://doi.org/10.1002/2017JC013023

Griffies, S., Biastoch, A., Boning, C., Bryan, F., Danabasoglu, G., Chassignet, E., et al. (2009). Coordinated Ocean-ice Reference Experiments (COREs). *Ocean Modelling*, *26*(1-2), 1–46. https://doi.org/10.1016/j.ocemod.2008.08.007

Hallberg, R. (2013). Using a resolution function to regulate parameterizations of oceanic mesoscale eddy effects. *Ocean Modelling*, *72*, 92–103. https://doi.org/10.1016/j.ocemod.2013.08.007

Harrison, C. S., Long, M. C., Lovenduski, N. S., & Moore, J. K. (2018). Mesoscale effects on carbon export: A global perspective. *Global Biogeochemical Cycles*, *32*, 680–703. https://doi.org/10.1002/2017GB005751

Hauck, J., Völker, C., Wolf-Gladrow, D. A., Laufkötter, C., Vogt, M., Aumont, O., et al. (2015). On the Southern Ocean CO_2 uptake and the role of the biological carbon pump in the 21st century. *Global Biogeochemical Cycles*, *29*, 2015GB005140. https://doi.org/10.1002/2015GB005140

Hausmann, U., McGillicuddy, D. J., & Marshall, J. (2017). Observed mesoscale eddy signatures in Southern Ocean surface mixed-layer depth. *Journal of Geophysical Research: Oceans*, *122*, 617–635. https://doi.org/10.1002/2016JC012225

Hunke, E. C., & Lipscomb, W. H. (2008). CICE: The Los Alamos Sea Ice Model. Documentation and software user's manual. Version 4.0. (*LA-CC-06-012*): Los Alamos National Laboratory.

Hurrell, J. W., Holland, M. M., Gent, P. R., Ghan, S., Kay, J. E., Kushner, P. J., et al. (2013). The Community Earth System Model: A framework for collaborative research. *Bulletin of the American Meteorological Society*, *94*(9), 1339–1360. https://doi.org/10.1175/BAMS-D-12-00121.1

Large, W. G. (1998). Modeling and parameterizing the ocean planetary boundary layer, *Ocean Modeling and Parameterization* pp. 81–120), NATO Science Series. Dordrecht: Springer. https://doi.org/10.1007/978-94-011-5096-53 en.

Large, W. G., McWilliams, J. C., & Doney, S. C. (1994). Oceanic vertical mixing: A review and a model with a nonlocal boundary layer parameterization. *Reviews of Geophysics*, *32*(4), 363–403. https://doi.org/10.1029/94RG01872

Large, W. G., & Yeager, S. (2004). Diurnal to decadal global forcing for ocean and sea-ice models: The data sets and flux climatologies. https://doi.org/10.5065/D6KK98Q6

Le Quéré, C., Bopp, L., & Tegen, I. (2002). Antarctic circumpolar wave impact on marine biology: A natural laboratory for climate change study. *Geophysical Research Letters*, *29*(10), 45–1-45-4. https://doi.org/10.1029/2001GL014585

Le Quéré, C., Buitenhuis, E. T., Moriarty, R., Alvain, S., Aumont, O., Bopp, L., et al. (2016). Role of zooplankton dynamics for Southern Ocean phytoplankton biomass and global biogeochemical cycles. *Biogeosciences*, *13*(14), 4111–4133. https://doi.org/10.5194/bg-13-4111-2016

Lehahn, Y., d'Ovidio, F., Lévy, M., Amitai, Y., & Heifetz, E. (2011). Long range transport of a quasi isolated chlorophyll patch by an Agulhas ring. *Geophysical Research Letters*, *38*, L16610. https://doi.org/10.1029/2011GL048588

Lima, I. D., Lam, P. J., & Doney, S. C. (2014). Dynamics of particulate organic carbon flux in a global ocean model. *Biogeosciences*, *11*(4), 1177–1198. https://doi.org/10.5194/bg-11-1177-2014

Long, M. C., Lindsay, K., Peacock, S., Moore, J. K., & Doney, S. C. (2013). Twentieth-century oceanic carbon uptake and storage in CESM1(BGC). *Journal of Climate*, *26*(18), 6775–6800. https://doi.org/10.1175/JCLI-D-12-00184.1

Mahadevan, A., Thomas, L. N., & Tandon, A. (2008). Comment on "Eddy/wind interactions stimulate extraordinary mid-ocean plankton blooms". *Science*, *320*(5875), 448; author reply 448. https://doi.org/10.1126/science.1152111

Marinov, I., Gnanadesikan, A., Sarmiento, J. L., Toggweiler, J. R., Follows, M. J., & Mignone, B. K. (2008). Impact of oceanic circulation on biological carbon storage in the ocean and atmospheric pCO_2. *Global Biogeochemical Cycles*, *22*, GB3007. https://doi.org/10.1029/2007GB002958

Martin, A., & Richards, K. J. (2001). Mechanisms for vertical nutrient transport within North Atlantic mesoscale eddy. *Deep-sea Research Part Ii-topical Studies in Oceanography - DEEP-SEA RES PT II-TOP ST OCE*, *48*, 757–773. https://doi.org/10.1016/S0967-0645(00)00096-5

McGillicuddy, D. J. (2016). Mechanisms of physical-biological-biogeochemical interaction at the oceanic mesoscale. *Annual Review of Marine Science*, *8*(1), 125–159. https://doi.org/10.1146/annurev-marine-010814-015606

McGillicuddy, D. J., Anderson, L. A., Bates, N. R., Bibby, T., Buesseler, K. O., Carlson, C. A., et al. (2007). Eddy/wind interactions stimulate extraordinary mid-ocean plankton blooms. *Science*, *316*(5827), 1021–1026. https://doi.org/10.1126/science.1136256

McGillicuddy, D. J., Anderson, L. A., Doney, S. C., & Maltrud, M. E. (2003). Eddy-driven sources and sinks of nutrients in the upper ocean: Results from a 0.1° resolution model of the North Atlantic. *Global Biogeochemical Cycles*, *17*(2), 1035. https://doi.org/10.1029/2002GB001987

McGillicuddy, D. J., Robinson, A. R., Siegel, D. A., Jannasch, H. W., Johnson, R., Dickey, T. D., et al. (1998). Influence of mesoscale eddies on new production in the Sargasso Sea. *Nature*, *394*(6690), 263. https://doi.org/10.1038/28367

Meredith, M. P. (2016). Understanding the structure of changes in the Southern Ocean eddy field. *Geophysical Research Letters*, *43*, 5829–5832. https://doi.org/10.1002/2016GL069677

Misumi, K., Lindsay, K., Moore, J. K., Doney, S. C., Bryan, F. O., Tsumune, D., & Yoshida, Y. (2014). The iron budget in ocean surface waters in the 20th and 21st centuries : Projections by the Community Earth System Model version 1. https://doi.org/10.5194/bg-11-33-2014

Moore, J. K., & Abbott, M. R. (2002). Surface chlorophyll concentrations in relation to the Antarctic Polar Front: Seasonal and spatial patterns from satellite observations. *Journal of Marine Systems*, *37*(1), 69–86. https://doi.org/10.1016/S0924-7963(02)00196-3

Moore, J. K., & Braucher, O. (2008). Sedimentary and mineral dust sources of dissolved iron to the world ocean. *Biogeosciences*, *5*(3), 631–656. https://doi.org/10.5194/bg-5-631-2008

Moore, J. K., Doney, S. C., Glover, D. M., & Fung, I. Y. (2001). Iron cycling and nutrient-limitation patterns in surface waters of the World Ocean. *Deep Sea Research Part II: Topical Studies in Oceanography*, *49*(1), 463–507. https://doi.org/10.1016/S0967-0645(01)00109-6

Moore, J. K., Doney, S. C., & Lindsay, K. (2004). Upper ocean ecosystem dynamics and iron cycling in a global three-dimensional model. *Global Biogeochemical Cycles*, *18*, GB4028. https://doi.org/10.1029/2004GB002220

Moore, J. K., Lindsay, K., Doney, S. C., Long, M. C., & Misumi, K. (2013). Marine ecosystem dynamics and biogeochemical cycling in the Community Earth System Model [CESM1(BGC)]: Comparison of the 1990s with the 2090s under the RCP4.5 and RCP8.5 Scenarios. *Journal of Climate*, *26*(23), 9291–9312. https://doi.org/10.1175/JCLI-D-12-00566.1

Nelson, D. M., & Smith, W. 0. (1991). Sverdrup revisited: Critical depths, maximum chlorophyll levels, and the control of Southern Ocean productivity by the irradiance-mixing regime. *Limnology and Oceanography*, *36*(8), 1650–1661. https://doi.org/10.4319/lo.1991.36.8.1650

O'Neill, L. W., Chelton, D. B., & Esbensen, S. K. (2010). The effects of SST-induced surface wind speed and direction gradients on midlatitude surface vorticity and divergence. *Journal of Climate*, *23*(2), 255–281. https://doi.org/10.1175/2009JCLI2613.1

Pujol, M.-I., Faugère, Y., Taburet, G., Dupuy, S., Pelloquin, C., Ablain, M., & Picot, N. (2016). DUACS DT2014: The new multi-mission altimeter data set reprocessed over 20 years. *Ocean Science*, *12*(5), 1067–1090. https://doi.org/10.5194/os-12-1067-2016

Rohr, T., Harrison, C., Long, M. C., Gaube, P., & Doney, S. C. (2020). The simulated biological response to Southern Ocean eddies via biological rate modification and physical transport. *Global Biogeochemical Cycles*, *34*, e2019GB006385. https://doi.org/10.1029/2019GB006385

Rohr, T., Long, M., T. Kavanaugh, M., Lindsay, K., & Doney, S. (2017). Variability in the mechanisms controlling Southern Ocean phytoplankton bloom phenology in an ocean model and satellite observations. *Global Biogeochemical Cycles*, *31*, 922–940. https://doi.org/10.1002/2016gb005615

Schoemann, V., Becquevort, S., Stefels, J., Rousseau, V., & Lancelot, C. (2005). Phaeocystis blooms in the global ocean and their controlling mechanisms: A review. *Journal of Sea Research*, *53*, 43–66. https://doi.org/10.1016/j.seares.2004.01.008

Siegel, D. A., McGillicuddy, D. J., & Fields, E. A. (1999). Mesoscale eddies, satellite altimetry, and new production in the Sargasso Sea. *Journal of Geophysical Research*, *104*(C6), 13,359–13,379. https://doi.org/10.1029/1999JC900051

Smith, R., Jones, P., Briegleb, P., Bryan, O., Danabasoglu, G., Dennis, M., et al. (2010). The Parallel Ocean Program (POP) reference manual: Ocean component of the Community Climate System Model (CCSM).

Song, H., Long, M. C., Gaube, P., Frenger, I., Marshall, J., & McGillicuddy, D. J. (2018). Seasonal variation in the correlation between anomalies of sea level and chlorophyll in the Antarctic circumpolar current. *Geophysical Research Letters*, *45*, 5011–5019. https://doi.org/10.1029/2017GL076246

Stevens, D. P., & Killworth, P. D. (1992). The distribution of kinetic energy in the Southern Ocean: A comparison between observations and an eddy resolving general circulation model. *Philosophical Transactions of the Royal Society of London. Series B*, *338*(1285), 251–257 en. https://doi.org/10.1098/rstb.1992.0145

Tang, K. W., Smith, W. O., Shields, A. R., & Elliott, D. T. (2009). Survival and recovery of Phaeocystis antarctica (Prymnesiophyceae) from prolonged darkness and freezing. *Proceedings of the Royal Society of London B: Biological Sciences*, *276*(1654), 81–90. https://doi.org/10.1098/rspb.2008.0598

Uitz, J., Claustre, H., Morel, A., & Hooker, S. B. (2006). Vertical distribution of phytoplankton communities in open ocean: An assessment based on surface chlorophyll. *Journal of Geophysical Research*, *111*, C08005. https://doi.org/10.1029/2005JC003207

van der Ploeg, R. R., Bohm, W., & Kirkham, M. B. (1999). On the origin of the theory of mineral nutrition of plants and the law of the minimum. *Soil Science Society of America Journal*, *63*(5), 1055–1062. https://doi.org/10.2136/sssaj1999.6351055x

Venables, H. J., & Meredith, M. P. (2009). Theory and observations of Ekman flux in the chlorophyll distribution downstream of South Georgia. *Geophysical Research Letters*, *36*, L23610. https://doi.org/10.1029/2009GL041371

Weijer, W., Sloyan, B. M., Maltrud, M. E., Jeffery, N., Hecht, M. W., Hartin, C. A., et al. (2011). The Southern Ocean and its climate in CCSM4. *Journal of Climate*, *25*(8), 2652–2675. https://doi.org/10.1175/JCLI-D-11-00302.1

Williams, S., Petersen, M., Bremer, P., Hecht, M., Pascucci, V., Ahrens, J., et al. (2011). Adaptive extraction and quantification of geophysical vortices. *IEEE Transactions on Visualization and Computer Graphics*, *17*(12), 2088–2095. https://doi.org/10.1109/TVCG.2011.162

Zhang, S., Curchitser, N. E., Kang, D., A. Stock, C., & Dussin, R. (2018). Impacts of mesoscale eddies on the vertical nitrate flux in the Gulf Stream region. *Journal of Geophysical Research: Oceans*, *123*, 497–513. https://doi.org/10.1002/2017JC013402